JACS
JOURNAL OF THE AMERICAN CHEMICAL SOCIETY
Article
pubs.acs.org/JACS

Across the Structural Re-Entrant Transition in $BaFe_2(PO_4)_2$: Influence of the Two-Dimensional Ferromagnetism

Rénald David,[†] Alain Pautrat,[‡] Dmitry Filimonov,[§] Houria Kabbour,[†] Hervé Vezin,[∥] Myung-Hwan Whangbo,[⊥] and Olivier Mentré*,[†]

[†]Université Lille Nord de France, UCCS, UMR-CNRS 8181, ENSCL-USTL, Villeneuve d'Ascq, France
[‡]Laboratoire CRISMAT, UMR 6508-CNRS, ENSICAEN, Caen, France
[§]Department of Chemistry, Moscow State University, 119991 Moscow, Russia
[∥]Université Lille Nord de France, LASIR, UMR-CNRS 8516, USTL, Villeneuve d'Ascq, France
[⊥]Department of Chemistry, North Carolina State University, Raleigh, North Carolina 27695-8204, United States

Supporting Information

ABSTRACT: $BaFe_2(PO_4)_2$ was recently prepared by hydrothermal synthesis and identified as the first two-dimensional (2D) Ising ferromagnetic oxide, in which honeycomb layers made up of edge-sharing FeO_6 octahedra containing high-spin Fe^{2+} ions ($S = 2$) are isolated by PO_4 groups and Ba^{2+} cations. $BaFe_2(PO_4)_2$ has a trigonal R-3 structure at room temperature but adopts a triclinic P-1 structure below 140 K due to the Jahn–Teller (JT) instability arising from the $(t_{2g})^4(e_g)^2$ configuration. The triclinic crystal structure was refined to find significantly distorted $Fe^{2+}O_6$ octahedra in the honeycomb layers while the distortion amplitude Q_{JT} was estimated to 0.019 Å. The JT stabilization energy is estimated to be ~7 meV per formula unit by DFT calculations. Below ~70 K, very close to the ferromagnetic transition temperature T_c = 65.5 K, the structure of $BaFe_2(PO_4)_2$ returns to a trigonal R-3 structure in the presence of significant ferromagnetic domains. This rare re-entrant structural transition is accompanied by a discontinuous change in the quadrupolar splitting of Fe^{2+}, as determined by Mössbauer spectroscopy. EPR measurements show the presence of magnetic domains well above T_c, as expected for a ferromagnetic 2D Ising system, and support that the magnetism of $BaFe_2(PO_4)_2$ is uniaxial ($g_\perp = 0$).

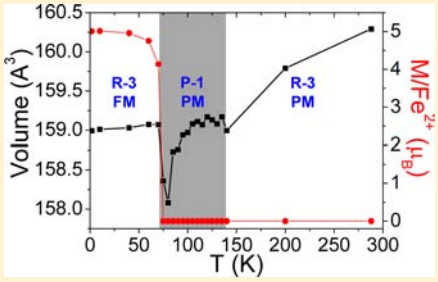

INTRODUCTION

Re-entrant structural transitions in crystalline solids as a function of temperature have been rarely observed in the absence of external stimulus such as pressure. The Rochelle salt, $NaKC_4H_4O_6{\cdot}4H_2O$, crystallizes in the space group $P2_12_12$ above 297 K and below 255 K, but exists in a distorted ferroelectric intermediate phase (space group $P2_111$) in the temperature region of 255–297 K.[1] Other well documented examples include malonitrile, $CH_2(CN)_2$,[2] and hybrid-layered perovskites $(C_3H_7NH_3)_2MnCl_4$.[3] Examples of purely inorganic materials are even more rare; to our knowledge, the ionic conductor $Ag_7P_3S_{11}$[4] and the rock-salt Li_2TiO_3[5] are the only known examples. The high-temperature γ-phase of $Ag_7P_3S_{11}$ (space group $C2/c$) with dynamical disorder of Ag^+ ions undergoes a phase transition at 205 K to an intermediate β-phase. At a temperature near 130 K, $Ag_7P_3S_{11}$ undergoes another phase transition, leading to an ordered low-temperature α-modification crystallizing in the same space group as the γ-phase. Li_2TiO_3 undergoes a first-order cation order–disorder transition through a metastable phase (space group $C2/c$) between the low and high temperature forms (space group Fm-3m) that differ in the Li/Ti ordering. For both compounds, the changes between the initial and final crystal structures involve re-entrant symmetries rather than re-entrant structural transitions. Our search for new isolated 2D layered-magnetic systems (e.g., *maple-leaf* lattice of Mn^{2+}, Mn^{3+}, and Mn^{4+} ions[6]) has recently led to $BaFe_2(PO_4)_2$ consisting of *honeycomb* layers made up of edge-sharing FeO_6 octahedra containing high-spin Fe^{2+} (d^6) ions. On cooling this oxide exhibits a striking re-entrant transition from the paramagnetic room-temperature (RT) form (space group R-3) to an intermediate paramagnetic phase (space group P-1) at 140 K and back to a R-3 ferromagnetic (FM) phase at 75K (near the ferromagnetic transition temperature T_c = 65.5K).[7] These transitions originate most likely from the Jahn–Teller (JT) instability of the FeO_6 octahedra containing high-spin Fe^{2+} ions; when each FeO_6 octahedron has a 3-fold rotational symmetry C_3, the high-spin Fe^{2+} ion induces both JT instability and uniaxial magnetism.[7,8] Since all FeO_6 octahedra are subject to JT instability, a cooperative JT (COJT) distortion should take place throughout the lattice, which will certainly affect the lattice phonons and hence elastic properties of the 3D lattice. However, it is difficult to quantify this relationship. As the lattice shrinks due to cooling, it might become difficult for certain systems to support a COJT distorted state, as found for

Received: May 10, 2013
Published: July 25, 2013

   dx.doi.org/10.1021/ja404697b | J. Am. Chem. Soc. 2013, 135, 13023–13029

$BaFe_2(PO_4)_2$ in the present study. The 2D Ising ferromagnetism for $BaFe_2(PO_4)_2$ arises from the uniaxial magnetism of the FeO_6 octahedra. When the temperature is lowered from the RT, the FeO_6 octahedra undergo a JT distortion at 140 K but this distortion is suppressed below 75 K, which is due probably to the excessive thermal contraction of the lattice. In the present work, we analyze the competition between the JT instability and the uniaxial magnetism in $BaFe_2(PO_4)_2$ by examining its crystal structure and its magnetic structure by powder neutron diffraction (PND), EPR, and Mössbauer measurements as a function of temperature. DFT calculations also bring significant insights into the relative stabilities of the competing crystallographic phases.

EXPERIMENTAL SECTION

While we have intensively discussed the preparation of $BaFe_2(PO_4)_2$ and evidence for its 2D-Ising ferromagnetism in ref 7, this paper includes a set of novel experiments performed across the re-entrant transition mentioned above and others only briefly discussed in our prior work.

Synthesis. $BaFe_2P_2O_8$ crystals were obtained by hydrothermal synthesis (220 °C) with hydrazine as reducing agent in the feeding solution containing $BaCO_3/FeCl_2.4H_2O$ (1.38g/1.39g) and H_3PO_4 (2 mL, 65%). The preparation of the powder samples was assisted by microwave; see ref 7 for details.

Structural Investigation. XRD measurements of a 100 K single-crystal XRD sample were carried out on a Duo Bruker SMART APEX diffractometer using Mo Kα radiation. Diffraction intensities were extracted and corrected for Lorentz and Polarization. An empirical absorption correction was then applied using the SADABS program,[9] and the refinement was processed using Jana 2006.[10] High-resolution powder neutron diffraction analysis was carried out at the LLB. Data were collected with the G41 (λ = 2.4226 Å) diffractometer. Refinements were carried out using the Fullprof program.[11]

^{57}Fe Mössbauer Spectroscopy. It was performed in a transmission mode using a constant acceleration spectrometer coupled with liquid helium or nitrogen cryostats. A ^{57}Co/Rh γ-ray source, maintained at room temperature, was used for the measurements. The spectrometers were calibrated with standard α-Fe or sodium nitroprusside absorbers. All isomer shift values (IS) are referred to α-Fe. A static spin Hamiltonian approach was utilized to analyze the spectra, where the fitting parameters were IS, electric quadrupole splitting ΔE_Q, magnetic hyperfine field (H_{hf}), the polar angles between H_{hf} and the principle axis of the EFG tensor Θ, asymmetry parameter of the EFG η. Note that the polar angle Θ was found to be zero within experimental error, namely H_{hf} is collinear to the principal axis of the EFG, and thus the azimuthal angle of H_{hf} has no impact on the line shape and was not refined. The values of the asymmetry parameter η should be regarded as rough estimates because their effect is indeed small for the current combinations of the hyperfine parameters, and was more obscured by the presence of impurities.

EPR. X-band EPR experiments were carried out with a Bruker ELEXYS E580E spectrometer. Microwave power and modulation amplitude were respectively 1 mW and 5 G. The spectra were recorded between 120 and 60 K using helium ITC503 oxford temperature regulation.

Density Functional Theory (DFT) Calculations. Using the Vienna ab initio simulation package,[12] our calculations were carried out within the generalized gradient approximation (GGA) for the electron exchange and correlation corrections using the Perdew–Wang[13] functional and the frozen core augmented wave method.[14] The total energies of the optimized structures were calculated using a plane wave energy cutoff of 400 eV, a total energy convergence threshold of 10^{-6} and 115 k points (99 k points) in the irreducible Brillouin zone for the rhombohedral structure (triclinic structure).

RESULTS AND DISCUSSION

The Triclinic Distortion. The re-entrant structural transition was first evidenced by means of high resolution powder neutron diffraction data (PND) collected at the Laboratoire Leon Brillouin using the high resolution G41 diffractometer (λ=2.4226 Å) from 288 to 1.8 K.[7] The splitting of the diffraction peaks below 140 K and coalescence on further cooling at 70 K is shown in Figure 1a. The correspondence between the *R*-3 and *P*-1 lattice is given by the relations: $a_{tricl} = -b_{rhombo}$, $b_{tricl} = a_{rhombo}$, $c_{tricl} = -1/3a_{rhombo} + 1/3b_{rhombo} + 1/3c_{rhombo}$. The evolution of the lattice parameters across the re-entrant transition in the triclinic setting is shown in Figure 1b. The correspondence between the two cells is shown in Figure 1c. From the evolution of the individual lattice parameters across the re-entrant transition, it follows that the *R*-3 → *P*-1 transition is accompanied by a concave upward volume $V(T)$ contraction on cooling, from 140 to 70 K. At 70 K, on the *P*-1→ *R*-3 transition, the cell volume is suddenly dilated. The lattice parameters remain nearly unchanged in the low-temperature rhombohedral domain from 70 to 1.8 K. This strong contraction effect is most probably at the origin of the transition, as explained below. By defining a volumic contraction coefficient on cooling as $\alpha_V = 1/V_0(dV/dT)$, we obtain the average values $\alpha_{V(RT\text{-}160K)} = 62 \times 10^{-6}$ K^{-1}, $\alpha_{V(105-80K)} = 251 \times 10^{-6}$ K^{-1}, and $\alpha_{V(70-2K)} = 7.3 \times 10^{-6}$ K^{-1}. These values show an inhomogeneous behavior in the three structural/magnetic states.

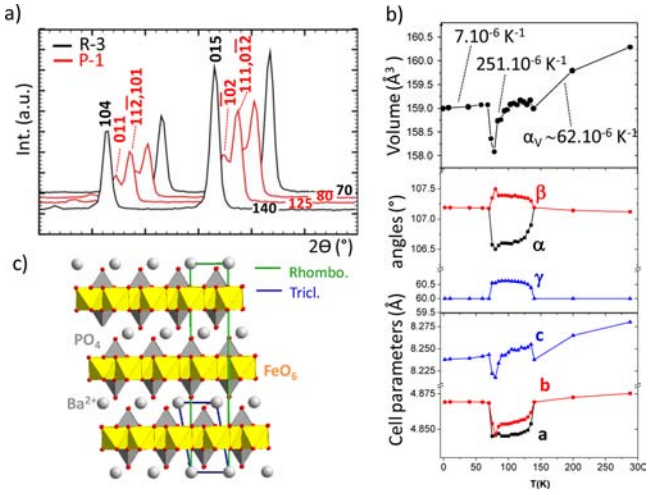

Figure 1. (a) Split of the 104 and 015 (trigonal) reflections below 140 K and re-entrant transition at 70 K from PND (λ = 2.4226 Å). (b) Evolution of the cell parameters across the re-entrant transition (triclinic setting). (c) Correspondence between the *R*-3 and the *P*-1 unit cells.

Data from a single crystal were collected at 100 K, and the triclinic crystal structure was subsequently refined (for details, see Table S1 of the Supporting Information). The unit cell parameters refined from the full data set are a = 4.8584(8) Å, b = 4.8656(8) Å, c = 8.248(1) Å, α = 72.988(7)°, β = 73.15(7)°, γ = 60.333(7)°. It was refined in the *P*-1 space group with final residuals factors $R_{(all)}$ = 2.18%, $_WR_{(all)}$ = 2.38% (refined anisotropic temperature parameters and atom positions are listed in Tables S2 and 3). The cell-distortion is accompanied by a twinning in two major domains related by a rotation of 180° around [010] as determined using the program CELL

dx.doi.org/10.1021/ja404697b | J. Am. Chem. Soc. 2013, 135, 13023–13029

Table 1. Experimental Details, Cell Parameters, Magnetic Moment, Interatomic Distances (Å), and *R* Factors for Structure Refined at Different Temperatures

method		S.Crystal	PND	S.Crystal	PND	PND	PND	PND	PND
T (K)		293	288	100	70	60	40	10	1.8
SG		*R*-3	*R*-3	*P*-1	*R*-3	*R*-3	*R*-3	*R*-3	*R*-3
a (Å)/*α* (°)		4.8730(2)	4.874(4)	4.8656(8)/ 106.85(1)	4.868(6)	4.869(3)	4.869(4)	4.869(4)	4.869(3)
b (Å)/*β* (°)		4.8730(2)	4.874(4)	4.8584(8)/ 107.01(1)	4.868(6)	4.869(3)	4.869(4)	4.869(4)	4.869(3)
c (Å)/*γ* (°)		23.368(2)	23.356(7)	8.248(1)/ 60.33(1)	23.248(3)	23.241(6)	23.235(5)	23.231(7)	23.230(2)
$M_{(Fe)}$ (μ_B)					4.285	4.972	5.223	5.291	5.289
Fe	O2			2.086(6)					
	O2	3 × 2.114(5)	3 × 2.11(1)	2.127(5)	3 × 2.11(1)	3 × 2.12(1)	3 × 2.12(1)	3 × 2.12(1)	3 × 2.11(1)
	O3			2.112(4)					
	O4			2.115(4)					
	O3	3 × 2.140(5)	3 × 2.15(1)	2.129(5)	3 × 2.14 (1)	3 × 2.14(1)	3 × 2.14(1)	3 × 2.13 (1)	3 × 2.13(1)
	O4			2.151(6)					
P	O1	3 × 1.554(5)	3 × 1.56(1)	1.505(4)	3 × 1.58(4)	3 × 1.57(2)	3 × 1.57(1)	3 × 1.57(2)	3 × 1.57(1)
	O3	1.538(7)	1.46(3)	1.558(6)	1.49(3)	1.48(2)	1.48(3)	1.48(3)	1.48(2)
	O2			1.561(4)					
	O4			1.566(7)					
Ba	O1			2 × 2.859(7)					
	O1	6 × 2.874(1)	6 × 2.86(1)	2 × 2.883(5)	6 × 2.86(1)	6 × 2.86 (1)	6 × 2.86 (1)	6 × 2.86 (1)	6 × 2.86(1)
	O1			2 × 2.886(5)					
Fe	Fe			2.729(2)					
	Fe	3 × 2.8181(2)	3 × 2.82(2)	2.8217(2)	3 × 2.82(1)	3 × 2.82(1)	3 × 2.82(2)	3 × 2.82(2)	3 × 2.82(1)
	Fe			2.899(2)					
R factor		*R* = 4.03%	R_{Bragg} = 3.34	*R* = 2.15%	R_{Bragg} = 3.32% R_{Magn} = 5.43%	R_{Bragg} = 3.62% R_{Magn} = 5.33%	R_{Bragg} = 3.59% R_{Magn} = 5.38%	R_{Bragg} = 3.53% R_{Magn} = 5.11%	R_{Bragg} = 3.83% R_{Magn} = 5.17%

NOW.[15] The pertinent distances at room-temperature (*R*-3 form) and at 100 K (*P*-1 form) are given in Table 1 from single crystal data, which shows six Fe−O bonds ranging from 2.086(6) to 2.152(6) Å. Below the *P*-1 → *R*-3 transition, the crystal structures have been refined from PND data blocking thermal parameters to B = 0.5 Å^2 for all atoms, together with the refinement of the magnetic moment. Despite the rather short angular domain provided by the wavelength λ=2.4226 Å, results are reliable taking into account the small number of structural and magnetic parameters to refine (6 + 1) in the rhombohedral geometry with uniaxial moments. It was checked that at room temperature the PND-data refinement gives Fe−O bond distances similar to those refined from single crystal (Fe and O having large neutron scattering lengths); see Table 1. But one can notice that, for P−O distances, in the neutron case P−O3 is systematically shorter than P−O1, whereas for the X-ray case these distances are similar. It most probably pictures a less accurate refinement in the interleave space due to comparable Fermi length of Ba and O atoms (O3 side) compared to "strongest contributing" Fe atoms (O1 side).

At least, in the *R*-3 low temperature domain, the crystal structure evolution is rather weak, in good agreement with the almost constant cell volume. The Rietveld patterns at 1.8 K are given in the Supporting Information (S4).

It is well-known that the JT effect associated with the t_{2g} orbital in an octahedral crystal field is weak. However, in the Verwey structure of the magnetite Fe_3O_4, it was recently established by high energy XRD that the JT distortion participates into the Fe^{2+}/Fe^{3+} octahedral charge ordering at low temperature.[16] In this ordered structure (space group *Cc*), JT active $Fe^{2+}O_6$ was identified on the basis of the magnitude of the JT active local modes (Q_{JT}). The maximal Q_{JT} components for the eight independent JT $-Fe^{2+}O_6$ octahedra were found between -0.026 Å < Q_{JT} < -0.058 Å and correspond in this case to a predominant tetragonal uniaxial distortion ($Q_{JT} = Q_T$). In the triclinic $BaFe_2(PO_4)_2$ at 100 K, we have estimated Q_{JT} as reported in ref 16 and detailed in the Supporting Information (S5). The three associated Eg symmetry amplitudes along *Qx*, *Qy*, and *Qz* of FeO_6 give $|Q_{O2-O3}|$ (= 0.0137 Å) > $|Q_{O3-O4}|$ (= -0.0112 Å) > $|Q_{O4-O2}|$ (= -0.0025 Å). The labels for the three axes are shown in Figure 3. It pictures the predominant orthorhombic (Q_O) but weaker tetragonal (Q_T) JT effects. Here we find the amplitudes $Q_{JT} = Q_O$ = 0.0187 Å, much greater than $Q_T = -0.005$ Å, contrary to what is observed in the Verwey structure of magnetite. However, in terms of amplitudes, in the title compound, one should consider weak JT distorsions.

In the distorted *honeycomb* layer of $BaFe_2(PO_4)_2$, the nearest-neighbor Fe−Fe distances are split into three distinct values from 2.729(2) to 2.899(2) Å. The distorted $Fe^{2+}O_6$ octahedra are arranged in zigzag alternated chains with short (2.73 Å) and medium Fe−Fe (2.82 Å) distances. The Fe−Fe distance between adjacent chains is ∼2.90 Å at 100 K. Finally, the interlayer distance between two adjacent layers remains nearly unchanged, 7.76 Å at 100 K against 7.79 Å at room temperature.

Other phases exhibiting the JT distortion of Fe^{2+} octahedral were reported in the literature, such as $FeSO_4$ $(H_2O)_6$.[17] This compound exhibits also disconnected 2D layers, and the asymmetry is discussed in relation with the static room temperature JT distortion. We can also cite the phosphate based $Ca_9Fe(PO_4)_7$ phase, with oxygen atoms all involved in phosphate groups[18] similarly to the title compound. While in oxides, a weak d^6 JT distortion could be easily suppressed by

dx.doi.org/10.1021/ja404697b | J. Am. Chem. Soc. 2013, 135, 13023−13029

small static or dynamic O^{2-} displacements; in phosphates, it is less straightforward and may be related to the observed phase transition, especially in a 2D type structure. It is also noteworthy to cite a Mössbauer theoretical study, in which accounting for dynamical JT coupling of high spin Fe^{2+} located in distorted octahedral of Fe-doped K_2ZnF_4 and Ba_2ZnF_6 improved the predictions compared to the static crystal field model.[19]

Magnetic Features. The magnetic data collected on a polycrystalline sample were reported in ref 7, which showed the effective moment of 6.16 μ_B/Fe^{2+} and the Curie–Weiss temperature θ_{cw} of 56.5 K. The effective moment has a significant contribution from the orbital moment because the spin-only effective moment is 4.9 μ_B/Fe^{2+} for a high-spin Fe^{2+} ion (S = 2). The P-1 → R-3 transition is accompanied by a weak anomaly in $\chi(T)$ at 140 K.[7] As the temperature lowered, the PND data show that the magnetic satellites around 70 K grow while T_c was accurately determined as 65.5 K from the fitting of the scaling-law equations. Due to the large separation between adjacent honeycomb layers, the interlayer interactions are very weak so that $BaFe_2(PO_4)_2$ is a nearly 2D FM magnet with critical exponent parameters around T_c: γ = 1.73(8), β = 0.12(7), and δ = 17(3).[7] The refinement of the magnetic structure led to a magnetic moment of 5.01(7) μ_B parallel to the c-axis at 1.8 K with final R-factor R_{Magn} = 5.38%. As determined from the PND at intermediate temperatures, the maximal moment is rapidly reached ($T \approx 60$ K), Figure 2a. The

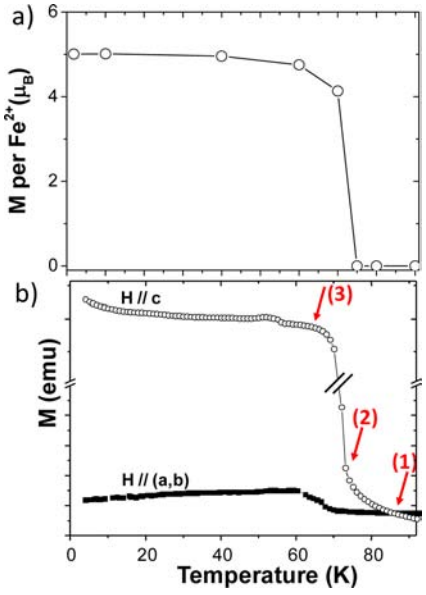

Figure 2. (a) Temperature-dependence of the magnetic moment per Fe^{2+} cation determined from PND refinements. (b) Temperature-dependence of the magnetic moments in the *ab*-plane M_{ab} (filled squares) and along the *c*-direction M_c (empty squares) measured on stacked single crystals: (1) anisotropic divergence of the magnetization below T = 85 K, (2) abrupt but continuous increase of M_c below T = 72 K, and (3) evaluated below T_c = 65.5 K.

accurate analysis of the $M(T)$ plots measured on a single crystal sample with applied field *along and perpendicular to c* show a divergence of $M_{(ab)}/M_{(c)}$ below 85 K, which is higher than T_c (Figure 2b). It indicates the occurrence of a significant thermal domain of short to medium range magnetic ordering. Below 90 K, $M_{(c)}$ increases abruptly but continuously despite the structural transition. It corresponds well to the features expected for the second order phase transition near the critical temperature of a 2D FM Ising system with a progressive enlargement of magnetic domains on cooling.[20]

The distortion of the honeycomb lattice leading to three different nearest-neighbor Fe–Fe distances is illustrated in Figure 3a. Our extended Hückel tight-binding calculations for a FeO_6 octahedron using the room-temperature rhombohedral structure show[7] that the low lying levels 1a and 1e are practically degenerate (Δe = 1.5 meV), and the high-spin state of the Fe^{2+} ion is described by two configurations $\Phi_1 = (1a)^2(1e)^2(2e)^2$ (L = 1, S = 2) and $\Phi_2 = (1a)^1(1e)^3(2e)^2$ (L = 2, S = 2). The latter configuration gives rise to uniaxial magnetism (i.e., unevenly filled degenerate level).[8] The FeO_6 octahedra in the 100 K crystal structure (P-1 space group) are significantly distorted and have no local C_3 rotational symmetry so that the t_{2g} and e_g levels of each FeO_6 octahedron are split, as indicated in Figure 3b; the d-block levels have no degeneracy

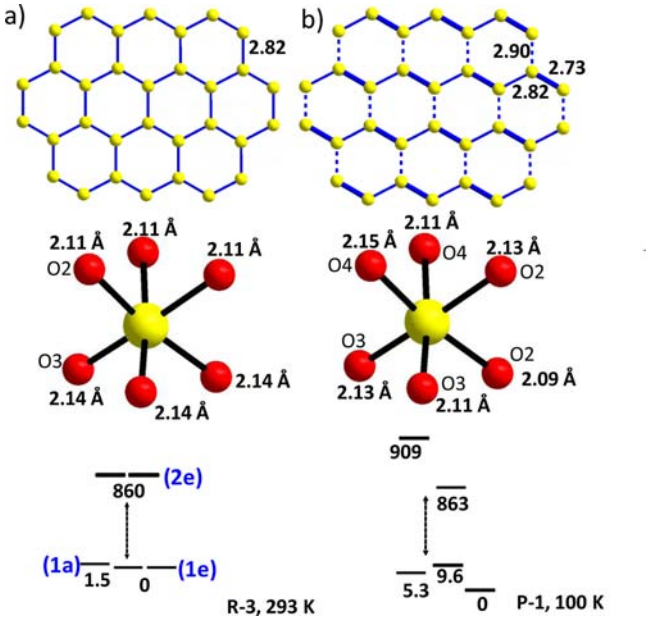

Figure 3. Fe-based honeycomb lattice (distances are in Å), FeO_6 geometry, and crystal field effect from extended Hückel calculations (the energy are given in meV) for (a) the rhombohedral symmetry at room temperature and (b) the triclinic symmetry at 100 K.

and hence cannot lead to an electron configuration responsible for uniaxial magnetism. The re-entrant transition below 70 K implies that, on further cooling below 70 K, the triclinic anisotropic contraction supporting the JT FeO_6 distortion becomes unfavorable, so the structure of $BaFe_2(PO_4)_2$ returns to the trigonal symmetry and hence to an uniaxial Ising magnetism.

Mössbauer Spectroscopy. The Mössbauer spectra of $BaFe_2(PO_4)_2$ were collected in the 4–300 K temperature range (Figure 4a). In the paramagnetic region, the spectra consist of single doublets with chemical isomer shifts (ISs) of >1.14 mm/s and narrow line widths, reflecting the presence of only one kind of Fe^{2+} cations in the structure. Below ~70 K (near T_c), the spectra magnetically split due to the FM ordering. It is noteworthy that all the spectra include two minor impurity components (about 4–5% each), which were included in the fitting models but, for simplicity, were not included in the summary of our analysis in Table 2.

dx.doi.org/10.1021/ja404697b | J. Am. Chem. Soc. 2013, 135, 13023–13029

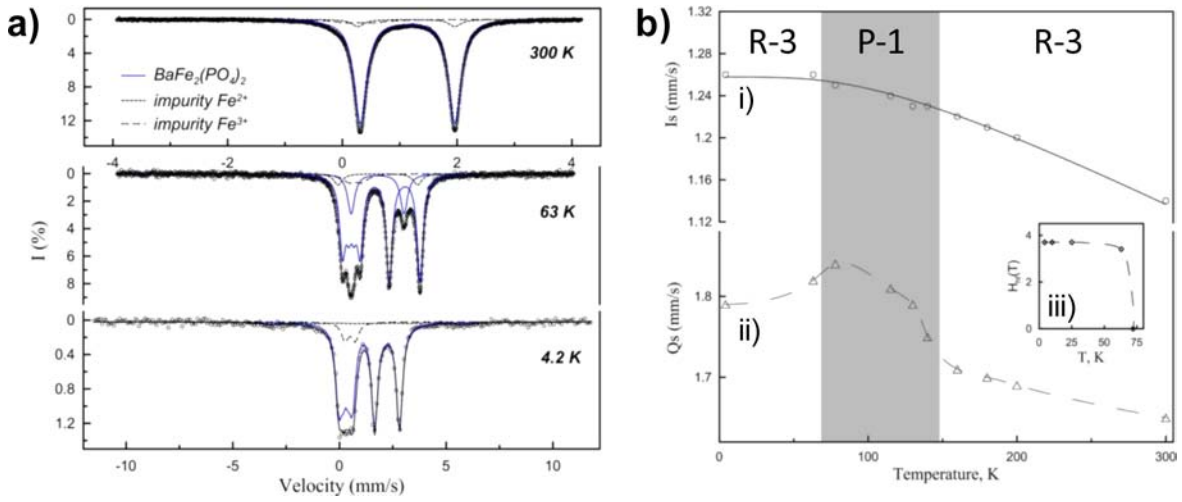

Figure 4. (a) Mössbauer spectra of $BaFe_2(PO_4)_2$. (b) Variation of the IS(T), QS(T), and $H_{hf}(T)$ of $BaFe_2(PO_4)_2$ as a function of T.

Table 2. ^{57}Fe Mössbauer Hyperfine Parameters of $BaFe_2(PO_4)_2$[a]

T, K	component	IS, mm/s ± 0.01	ΔE_Q, mm/s ± 0.01	H_{hf}, T ± 0.1	Θ, deg	η	Γ, mm/s ± 0.01	I, % ± 2
298	D11	1.14	1.65				0.26	89
78	D12	1.25	1.84				0.27	85
63	D13	1.24	1.84				0.30	73
	S11	1.26	1.82	3.4	0	~0.34	0.25	16
4.2	S12	1.26	1.79	3.7	0	~0.7	0.34	86

[a]IS, isomer shift relative to α-Fe at ambient temperature; ΔE_Q, electric quadrupole splitting; H_{hf}, magnetic hyperfine field, Θ, the polar angles between H_{hf} and the principle axis of the EFG tensor; η, asymmetry parameter of the EFG; Γ, line width; I, relative area.

The variation of the IS through the whole temperature range investigated is shown in the Figure 4b. In general, the IS consists of intrinsic isomer shift δ_i (temperature independent) and the second-order Doppler shift δ_D (temperature dependent), $\delta = \delta_i + \delta_D$. The latter is expressed in terms of the Debye approximation as follows:

$$\delta_D(T) = -\frac{9k_B\theta_M}{16Mc}\left[1 + 8\left(\frac{T}{\theta_M}\right)^4 \int_{\theta_M/T}^{0} \frac{x^3}{e^x - 1}\,dx\right]$$

where k_B is the Boltzmann constant, Mc is the weight of the ^{57}Fe nucleus, and Θ_M is the characteristic Mössbauer temperature related to the lattice Debye temperature. The latter can be evaluated from the experimental temperature dependence of IS. The solid line of the Figure 4b represents the fitted curve for IS with Θ_M refined as 444(19) K. This value is consistent with the Mössbauer temperatures (≥400 K) reported for ferrous phosphates and other compounds.[21,22]

The paramagnetic state of $BaFe_2(PO_4)_2$ shows a large quadrupole splitting (QS) of 1.65 mm/s at 300 K (Table 2), which increases with decreasing temperature. It is typical of the high-spin Fe^{2+} compounds with large 3d-electron contribution to the total electric field gradient (EFG). The temperature variation of the QS is shown in the Figure 4bii. At ~140 K where the triclinic $Fe^{2+}O_6$ octahedral distortion occurs, the QS exhibits a quick increase. The second bending of the QS(T) plot is observed at ~70 K (near T_c), followed by some decrease in the QS values. This reflects an increase in local symmetry of the FeO_6 octahedra, and, along with nonzero values of the asymmetry parameter η pointing out nonaxial distortion, is in good agreement with the re-entrant transition from P-1 to R-3. It is to note that, below T_c , QS values are close to ones extrapolated from the high-temperature R-3 domain similarly to the lattice parameters evolution at both sides of the triclinic domain (Figure 1b).

The Mössbauer spectra of $BaFe_2(PO_4)_2$ at temperatures below ~70 K are magnetically split (Figure 4a). The complicated shape of spectra are typical for the Fe^{2+} compounds with comparable strengths of the magnetic dipole and the electric quadrupole interaction. The $BaFe_2(PO_4)_2$ subspectra were fit with one single component with relatively narrow line width of <0.3 mm/s using a complete hyperfine interaction Hamiltonian (Table 2). The temperature variation of H_{hf} shows a sharp transition to the ferromagnetic state (Figure 4b), consistent with 2D FM structure of $BaFe_2(PO_4)_2$. However, at 3.7 T and 4.2 K, that is, close to the saturation point, the H_{hf} value is strikingly low compare to that in other Fe^{2+} phosphates and oxides: even though these values range widely because of high orbital and spin-dipolar contributions to hyperfine field, they generally exceed 10 T.[23,24] This low (almost saturated) H_{hf} is attributed to a fast spin relaxation involving easy down/up longitudinal and, presumably, an in-plane transverse relaxation of electron spins (LS coupling), related to 2D Ising type FM ordering. If the relaxation time τ_r is much less than the nuclear Larmor precession time τ_l (in iron phosphates, it is on the order of 10^{-8} s),[4] then the nucleus experiences a time averaged hyperfine field lower than the static values of H_{hf}, while narrow Lorentzian lines are still preserved. This is fully consistent with our typical $M(H)$ vs H plot at 4 K, which shows easy spin reversal without coercivity at $H \approx 0$ (2D Ising character).[7]

We now examine the triclinic to rhombohedral phase transition using spin-polarized GGA DFT calculations to determine the energies (i) E(PM, P-1) of the 100 K triclinic

dx.doi.org/10.1021/ja404697b | J. Am. Chem. Soc. 2013, 135, 13023−13029

crystal structure (P-1) and (ii) E(FM, R-3) of a model built using the R-3 room temperature structure for which the lattice parameters were extrapolated from Figure 1b so as to have exactly the same volume $V_{R\text{-}3} = V_{P\text{-}1}$. In such a way, the energy gained by the thermal contraction is neglected while the energy difference between both structures is due solely to the Jahn−Teller stabilization R-3 → P-1. We found E(FM, R-3) − E(FM, P-1) = ∼7 meV per formula unit (FU). This result indicates that the triclinic structure is slightly more stable than the rhombohedral one with an energy gain of ∼7 meV/FU due to the JT distortion.

EPR. Figure 5a shows the EPR spectra collected in the paramagnetic regime above and below the *rhombohedral* → *triclinic* transition temperature $T_t \approx 140$ K. All spectra are almost unchanged in this domain and lead to a major resonance at $g = 2.20$, assigned to $g_{\parallel}$ due to the local spin-anisotropy along c. It follows that the JT transition is accompanied with a minor change in $g_{\parallel}$, in good agreement with the weak $\chi(T)$ anomaly at the transition.[7] The $g_{\parallel}$ value denotes a significant spin−orbit coupling but cannot explain the important effective moment μ_{eff} = 6.16 μ_B/Fe^{2+} since the approximate $g\sqrt{S(S+1)}$ value tends to indicate an average $g \approx 2.5$. Then, one should consider a contribution of in-plane $g_{\perp}$ factor at least in the paramagnetic domain. The EPR spectra shows three minor resonances at g = 3.77, 3.55, and 1.27 (inset Figure 5a). They are most probably intrinsic to $BaFe_2(PO_4)_2$ since they vanish on further cooling below T_c. Their origin is still not understood, but one could imagine that $g_{\perp}$ is either 3.77 or 3.55, leading to a highest mean g value.

Even using a polycrystalline sample in the paramagnetic regime, a partial alignment of the grains easy axis along the applied magnetic field (H_{max} = 1 T) is efficient due to the magnetization of $BaFe_2(PO_4)_2$ that behaves as a 2D soft-ferromagnetic behavior with an almost zero coercitive field.[7] As shown in Figure 5a, a strong shift of the paramagnetic EPR spectra occurs below 90 K, which corresponds to the increase of the $M_{H\|c}(T)$ and creation of magnetic domains (see Figure 2b). Such a shift to a lower resonant field ($H_R \approx 3000$ G at 120 K against $H_R \approx 2700$ G at 90 K) is fully compatible with what was observed for other ferromagnetic systems.[25] The resonant field B_0 in the presence of ferromagnetic clusters is modified by an internal magnetic field B_{int} with respect to $h\nu = g\mu_B(B_0 - B_{int})$.[26] The observed shifts is related to the size of the magnetic domains and displaced toward lower applied B_0 as soon as magnetically active domains are created (i.e., when the material develops nonzero magnetization). As observed in our experimental magnetization measurements, magnetic clusters happen well above T_c = 65.5 K in accordance with the theoretical prediction of the 2D FM Ising magnetism.[27] To validate this hypothesis, we have collected EPR spectra at 90, 70, and 60 K during the increase and decrease of the magnetic field (0 → 1 T and 1 → 0 T, respectively).

Results are shown on the Figure 5b. Strong hysteretic effects are observed for the main absorption band, which show a resonance at lower field for the field-decreasing cycle (i.e., when domains are more strongly aligned). The amplitude of the hysteresis decreases on cooling (from ΔH_R = 175 G at T = 90 K to ΔH_R = 44 G at 60 K; see Figure 5b). It shows rather well the existence of robust ferromagnetic domains as high as 90 K. We also note that the minor resonances at g_1 = 3.77 and g_2 = 3.45 do not show hysteresis between the increasing- and decreasing-field cycles, suggesting their in-plane nature. As expected, the influence of the magnetic history of the sample below T_c is not strong any more since no significant hysteresis was observed. However, as shown in the inset of Figure 5b, the minor resonances at g_1 and g_2 do not persist below T_c , which validates the setting of uniaxial magnetism (significant $g_{\parallel}$, $g_{\perp}$ = 0).

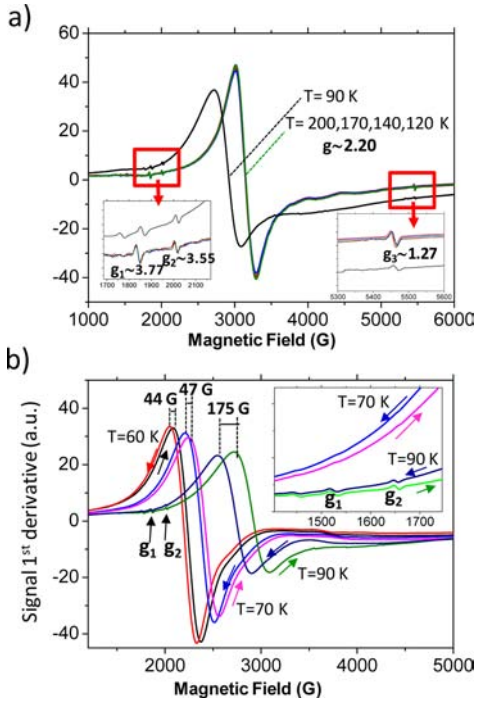

Figure 5. (a) EPR spectra collected on increasing the magnetic field (up) at various temperatures. For $T \geq 120$ K, no up/down hysteresis was observed leading to $g = 2.20$. Insets show the zoom of minor resonances g_1, g_2, and g_3. (b) Evidence of up/down EPR hysteresis between 60 and 90 K. Inset: vanishing of g_1 and g_2 below T_c.

CONCLUDING REMARKS

We investigated the re-entrant structural transitions, R-3 (paramagnetic) → P-1 (paramagnetic) → R-3 (ferromagnetic), of $BaFe_2(PO_4)_2$ in some detail. The JT instability observed below 140 K is accompanied by a triclinic distortion in which the FeO_6 octahedra lose their local C_3 rotation symmetry leading to six different Fe−O distances. This octahedral distortion is rather significant despite that the JT instability arises from the t_{2g} levels. On further cooling below ∼70 K, the JT distortion is no longer supported by the crystal lattice. Around this temperature, the system undergoes an abrupt cell dilatation and returns back to its initial rhombohedral symmetry. The low-temperature rhombohedral form is stabilized most probably by magnetostrictive effects that accompany the FM ordering with magnetic moments aligned along the c axis. At this transition, weak EPR resonances in the paramagnetic regime, which are assigned to the "in-plane" (a,b) phenomena, vanish. It is noteworthy that the magnetic behavior of a true 2D FM compound expected from the theory can be calculated at the critical point.[7] It was already shown that the value of T_c = 65.5 K matches well with the analytical solution T_c = 1.5186 J k_B for S = 2 ions in a honeycomb lattice. This T_c value was obtained using a FM J = 16.8 K calculated for the main Fe−O−Fe exchanges from GGA+U calculations (with U = 6 eV).[7] In addition, we show here that the progressive creation of magnetic domains across the second order magnetic

dx.doi.org/10.1021/ja404697b | J. Am. Chem. Soc. 2013, 135, 13023−13029

transition is well respected, since both magnetization and EPR data indicate an intrinsic nonzero magnetization well above T_c (T > ∼90 K) together with a continuous increase in $M_{H//c}$ despite the R-3 → P-1 transition. The low value of $H_{HF} \approx 3.7$ T at 4.2 K, as determined from Mössbauer spectroscopy, is well below the values observed for Fe^{2+} (H_{HF} > 10 T). This indicates that spin-reversal is easy in this 2D Ising system with almost zero coercivity.

■ ASSOCIATED CONTENT

Supporting Information

Single-crystal X-ray diffraction data, atomic positions, and thermal parameters of low temperature structure, Rietveld patterns at 1.8 K, and detail of QJT calculation. This material is available free of charge via the Internet at http://pubs.acs.org.

■ AUTHOR INFORMATION

Corresponding Author

olivier.mentre@ensc-lille.fr

Notes

The authors declare no competing financial interest.

■ ACKNOWLEDGMENTS

The Fonds Européen de Développement Régional (FEDER), CNRS, Région Nord Pas-de-Calais, and Ministère de l'Enseignement Supérieur et de la Recherche are acknowledged for funding of the X-ray diffractometers. R.D. thanks the ENS of Lyon for financial support. This work was carried out under the framework of the MAD-BLAST project supported by the ANR (Grant ANR-09-BLAN-0187-01).

■ REFERENCES

(1) (a) Beevers, C. A.; Hughes, W. *Proc. R. Soc. London, Ser. A* **1941**, *177*, 251. (b) Suzuki, E.; Shiozaki, Y. *Phys. Rev. B* **1996**, *53*, 5217.

(2) (a) Wasiutynski, T.; Olejarczyk, W.; Sciesinski, J.; Witko, W. *J. Phys. C* **1987**, *20*, L65. (b) Dove, M. T. *J. Phys.: Condens. Matter* **2011**, *23*, 225402.

(3) Brunskill, I. H.; Depmeier, W. *Acta Crystallogr., Sect. A* **1982**, *38*, 132.

(4) Brinkmann, C.; Eckert, H.; Wilmer, D.; Vogel, M.; Schmedt auf der Günne, J.; Hoffbauer, W.; Rau, F.; Pfitzner, A. *Solid State Sci.* **2004**, *6*, 1077.

(5) Leu, L.-C.; Bian, J.; Gout, D.; Letourneau, S.; Ubic, R. *RSC Adv.* **2012**, *2*, 1598.

(6) Aliev, A.; Huvé, M.; Colis, S.; Colmont, M.; Dinia, A.; Mentré, O. *Angew. Chem.* **2012**, *124*, 9527.

(7) Kabbour, H.; David, R.; Pautrat, A.; Koo, H.-J.; Whangbo, M.-H.; André, G.; Mentré, O. *Angew. Chem.* **2012**, *124*, 11915.

(8) (a) Dai, D.; Whangbo, M.-H. *Inorg. Chem.* **2005**, *44*, 4407. (b) Zhang, Y.; Xiang, H. J.; Whangbo, M.-H. *Phys. Rev. B* **2009**, *79*, 054432. (c) Zhang, Y.; Kan, E. J.; Xiang, H. J.; Villesuzanne, A.; Whangbo, M.-H. *Inorg. Chem.* **2011**, *50*, 1758.

(9) (a) *SAINT: Area-Detector Integration Software*; Siemens Industrial Automation, Inc.: Madison, WI, 1995. (b) *SADABS: Area-Detector Absorption Correction*; Siemens Industrial Automation, Inc.: Madison, WI, 1996.

(10) Petricek, V.; Dusek, M.; Palatinus, L. *JANA2000: The Crystallographic Computing System*; Institute of Physics: Praha, Czech Republic, 2000.

(11) Rodriguez-Carvajal, J. *Phys. B* **1993**, *192*, 55 (program Fullprof available from http://www-llb.cea.fr/fullweb/fp2k/fp2k.htm.

(12) Kresse, G.; Furthmüller, J. *Vienna Ab-initio Simulation Package (VASP)*; Institut für Materialphysik: Vienna, 2008; http://cms.mpi.univie.ac.at/vasp.

(13) Perdew, J. P.; Wang, Y. *Phys. Rev. B* **1992**, *45*, 13244.

(14) Kresse, G.; Joubert, D. *Phys. Rev. B* **1999**, *59*, 1758.

(15) Sheldrick, G. M. *CELL NOW, program for unit cell determination*; Göttingen University: Göttingen, Germany; http://shelx.uni-ac.gwdg.de/SHELX.

(16) Senn, M. S.; Wright, J. P.; Attfield, J. P. *Nature* **2012**, *481*, 173.

(17) Gutlich, P.; Garcia, Y. *Chemical Applications of Mössbauer Spectroscopy, in Mössbauer Spectroscopy, Tutorial Book*; Yoshida, Y., Langouche, G., Eds.; Springer: 2013, Vol. *308*, p 33.

(18) Benarafa, A.; Kacimi, M.; Gharbage, S.; Millet, J.-M.; Ziyad, M. *Mater. Res. Bull.* **2000**, *35*, 2047.

(19) Ducouret-Cereze, A.; Varret, F. *J. Phys. (Paris)* **1988**, *49*, 661.

(20) (a) Stanley, H. E. *Rev. Mod. Phys.* **1999**, *71*, S359. (b) Landau, D. P. *Phys. Rev. B* **1976**, *13*, 2997.

(21) Menil, F. *J. Phys. Chem. Solids* **1985**, *46*, 763.

(22) Van Alboom, A.; De Grave, E.; Wohlfahrt-Mehrens, M. *Am. Mineral.* **2011**, *96*, 408.

(23) Rhee, C. H.; Lee, I. K.; Moon, S. J.; Kim, S. J.; Kim, C. S. *J. Korean Phys. Soc.* **2011**, *58*, 472.

(24) Dickson, D. P. E., Berry, F. J., Eds. *Mössbauer Spectroscopy*; Cambridge University Press: Cambridge, 1986.

(25) (a) Guskos, N.; Typek, J.; Zolnierkiew, G.; Blonska-Tabero, A.; Los, S.; Kempinski, W. *Mater. Sci.-Pol.* **2006**, *24*, 983. (b) Atsarkin, V. A.; Demidov, V. V. *J. Exp. Theor. Phys.* **2006**, *103*, 589.

(26) (a) Koskarov, Y. A.; Pankratov, D. A.; Gubin, S. P.; Kosobudsky, I. D.; Beltran, M.; Khodorkvsky, Y.; Tishin, A. M. *J. Appl. Phys.* **2001**, *89*, 2293. (b) Guskos, N.; Anagnostakis, E. A.; Likodimos, V.; Bodziony, T.; Typek, J.; Maryniak, M.; Narkiewicz, U.; Kucharewicz, I. *J. Appl. Phys.* **2005**, *97*, 024304.

(27) Da Silva, P. C.; Fulco, U. L.; Nobre, F. D.; Da Silva, L. R.; Lucena, L. S. *Braz. J. Phys.* **2002**, *32*, 617.